KeAi
CHINESE ROOTS
GLOBAL IMPACT

Available online at www.sciencedirect.com

ScienceDirect

Green Energy & Environment 5 (2020) 461–472

www.keaipublishing.com/gee

Research paper

Core-shell particles of C-doped CdS and graphene: A noble metal-free approach for efficient photocatalytic H_2 generation

Muhammad Zubair [a], Estelle Marie M. Vanhaecke [a], Ingeborg-Helene Svenum [a,b], Magnus Rønning [a], Jia Yang [a,*]

[a] *Department of Chemical Engineering, Norwegian University of Science and Technology (NTNU), Sem Sælands vei 4, Trondheim, NO, 7491, Norway*
[b] *SINTEF Industry, P. O. Box 4760 Torgarden, Trondheim, NO, 7465, Norway*

Received 20 July 2020; revised 13 October 2020; accepted 13 October 2020
Available online 17 October 2020

Abstract

To achieve efficient photocatalytic H_2 generation from water using earth-abundant and cost-effective materials, a simple synthesis method for carbon-doped CdS particles wrapped with graphene (C-doped CdS@G) is reported. The doping effect and the application of graphene as co-catalyst for CdS is studied for photocatalytic H_2 generation. The most active sample consists of CdS and graphene (CdS-0.15G) exhibits promising photocatalytic activity, producing 3.12 mmol g^{-1} h^{-1} of H_2 under simulated solar light which is ~4.6 times superior than pure CdS nanoparticles giving an apparent quantum efficiency (AQY) of 11.7%. The enhanced photocatalytic activity for H_2 generation is associated to the narrowing of the bandgap, enhanced light absorption, fast interfacial charge transfer, and higher carrier density (N_D) in C-doped CdS@G samples. This is achieved by C doping in CdS nanoparticles and the formation of a graphene shell over the C-doped CdS nanoparticles. After stability test, the spent catalysts sample was also characterized to investigate the nanostructure.

Keywords: C-doped CdS@G; Core-shell nanostructure; Photocatalytic H_2 generation; Graphene; Carbon doping in CdS; Bandgap narrowing

1. Introduction

To overcome the current environmental issues and energy crisis, renewable and inexhaustible solar energy can be utilized to meet the increasing energy demands [1]. Photocatalytic H_2 generation from water is considered as a "holy grail" which can harness the solar energy and store this energy in the form of H_2 and O_2 [2]. From the perspective of photocatalytic H_2 generation from water, cadmium sulfide (CdS) is considered as an interesting candidate having a narrow bandgap of ~2.4 eV. It can absorb broader solar spectrum and contains suitable band edge positions that fulfill the thermodynamic requirements for water splitting. Despite having captivating characteristics, high photo-excited charge recombination and self-photocorrosion due to unconsumed holes (h^+) in the valence band of CdS, restricts its practical applications at current stage [3]. To overcome the mentioned bottlenecks, different approaches including noble metal loading as co-catalysts on CdS, heterojunction formation, and doping of CdS with different elements have been investigated [4]. Still, a significant amount of work is needed to further improve the activity and stability of CdS to generate higher amount of photocatalytic H_2 from water.

Graphene, a 2-D material having sp^2-hybridized carbon, exhibits high charge mobility and thus is considered as a promising co-catalyst for photocatalytic applications [5]. The presence of graphene as co-catalyst decreases the charge recombination and increases charge separation which in turn gives improved photocatalytic efficiency for H_2 generation

* Corresponding author.
E-mail address: jia.yang@ntnu.no (J. Yang).

https://doi.org/10.1016/j.gee.2020.10.017

without using noble metals [6]. Han et al. have recently described that the oxygen-containing groups on carbon quantum dots played an important role in degrading organic pollutant efficiently employing light [7]. Zeng et al. has reported enhanced apparent quantum efficiency of 10.4% shown by CdS with the use of reduced graphene oxide as co-catalyst which extracts the electrons from the photoexcited CdS [8]. Li et al. has synthesized visible light active CdS-graphene sheets by a solvothermal method and applied it in photocatalytic H_2 generation using Pt as co-catalysts. The enhanced photocatalytic H_2 generation is caused by the improved charge separation by the use of two co-catalysts, *i.e.* graphene and Pt [6]. These reports suggest that graphene with oxygen-containing groups can act as a co-catalyst for CdS-based photocatalysts for H_2 generation, but there is still a need to further boost activity and stability by applying graphene and CdS as a nanocomposite without using noble metals.

Doping is a compelling approach to manipulate the photoelectrochemical properties of the semiconductors. The incorporation of a dopant in CdS enhances the charge separation and also narrows down the bandgap of CdS to allow enhanced light absorption properties which in turn contributes to improving photocatalytic activity [9]. Furthermore, the dopant can introduce structural defects and new trapped states in CdS which are favorable for trapping e^- and h^+ resulting in spatial charge separation [10,11]. Shi et al. explained that the dopant in the CdS improves the photocatalytic activity due to less recombination and electron trapping by the dopant defects [12,13]. Numerous studies have described the effect of metal dopants [14–17] and non-metal dopants on the photocatalytic activity of CdS including P [13] and Se [18]. Also, carbon has been accepted as an effective dopant for various semiconductor materials to achieve an enhanced photocatalytic activity in *e.g.* TiO_2 [19], ZnO [20], ZrO_2 [21] and CdS [22]. Orlianges et al. have explained the effect of C-doping in CdS films which results in improved photoelectrochemical properties [23]. Ying et al. have also described the enhanced photocatalytic activity of C-doped CdS towards the degradation of RhB under solar simulated light due to higher carrier density and efficient charge separation [22]. The strategy of C-doping in CdS may have a positive effect on photocatalytic H_2 generation and should be further investigated.

The development of core-shell structures of C-doped CdS nanoparticles with graphene (C-doped CdS@G) may be a promising approach to attain increased activity and stability for light-induced H_2 evolution. The combined effect of doping and heterojunction formation between C-doped CdS and graphene by forming core-shell structure can be simultaneously manipulated to achieve elevated H_2 generation. By forming the core-shell nanostructure of graphene and C-doped CdS, photogenerated e^- and h^+ from the C-doped CdS can transfer towards graphene as the work function of graphene is less negative (−0.08 V *vs.* SHE) [24] than CdS, resulting in increased charge separation efficiency. An analogous observation was also reported by Bin et al. to avail improved photocatalytic activity towards the generation of H_2 by applying carbon-coated Cu^+-doped CdS nanocomposites [25]. Furthermore, the shell of graphene over C-doped CdS nanoparticles not only extract the charge carrier from the C-doped CdS but can also shield CdS from mechanical tension and photo-corrosion by efficiently neutralizing the photogenerated charge.

Motivated to investigate C-doping in CdS and wrapping of C-doped CdS with graphene (C-doped CdS@G) for photocatalytic H_2 generation, we report a simple method for the synthesis of C-doped CdS@G nanoparticles. First, the pure CdS nanoparticles and graphene quantum dots (GQD) are synthesized by a hydrothermal method and pyrolysis of citric acid, respectively. After that, core-shell structures of CdS@G were synthesized by adding varying quantity of GQD in CdS nanoparticles to optimize the graphene layer thickness. Finally, the C-doped CdS@G samples are formed by heat-treating the CdS@G sample at 400 °C in N_2 gas as shown in the synthesis scheme Fig. 1. The as-synthesized photocatalysts samples are extensively investigated by various characterization techniques along with electrochemical measurements. The activity of the catalysts is investigated by measuring their ability to generate H_2 from tap water or distilled tap water under simulated solar light.

2. Experimental part

2.1. Materials and reagents

For the synthesis of CdS nanoparticles, cadmium acetate dihydrate (98%) and thiourea (ACS. ≥ 99%) were purchased from Sigma-Aldrich and Alfa Aesar respectively. The citric acid (CA, ACS. ≥ 99.5%) and sodium hydroxide (≥99%) were ordered from Sigma-Aldrich and Millipore respectively, for the synthesis of GQD. Sodium sulfide nonahydrate ($Na_2S·9H_2O$, ACS. 98%) and anhydrous sodium sulfite (Na_2SO_3, 98%) used as hole scavengers in photocatalytic H_2 generation tests were procured from Alfa Aesar. Deionized (DI) water was utilized throughout the synthesis procedure.

2.2. Synthesis of pure CdS nanoparticles

The previously reported hydrothermal method [26] was applied for the synthesis of pure CdS nanoparticles. Briefly, a uniform solution of 5.26 g of thiourea and 1.8 g of cadmium acetate dihydrate was made in 60 ml of DI water. The resultant solution, after stirring for 10 min, was filled into a hydrothermal autoclave (volume = 90 mL) and kept this reactor at 180 °C for 18 h in a box furnace. After the completion of hydrothermal reaction, autoclave was allowed to cooldown naturally and CdS nanoparticles of orange color were obtained. After washing the CdS nanoparticles several times with DI water followed by drying at 80 °C for 12 h, pure CdS nanoparticles were collected.

2.3. Synthesis of pure graphene quantum dots (GQD)

A previously reported method by carbonization of citric acid (CA) [24,27] is used to synthesize the GQD. In short,

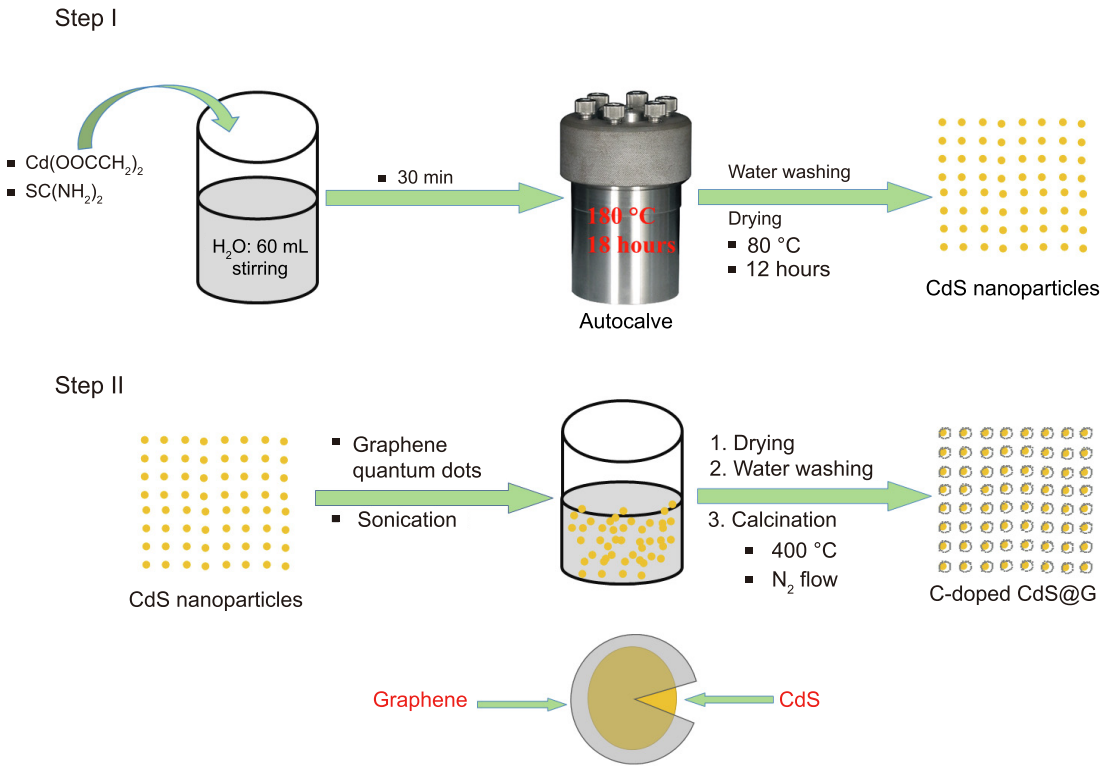

Fig. 1. Schematic illustration of the synthesis procedure of C-doped CdS@G samples.

citric acid (2 g) is melted at 180 °C in a glass vial until orange color of liquified citric acid appeared. The obtained liquid citric acid was added to 20 mL of aqueous NaOH solution (1g L^{-1}) under intense stirring. After cooling down, a suspension of GQD with ~100 mg mL^{-1} concentration was obtained and comprehensive characterization has already been reported in previous research papers [24,27–29].

2.4. Synthesis of carbon-doped CdS@graphene samples (C-doped CdS@G)

For the synthesis of C-doped CdS@G samples, 300 mg of CdS nanoparticles, a varying amount of GQD solution (mL), and 2 mL of DI water were placed in a test tube and sonicated for 30 min to make a uniform mixture. After sonication, the suspension was dried overnight at 80 °C in an electric oven. The dried mixture of CdS and GQD was then ground and placed in a glass reactor and was heat treated at 400 °C for 1 h under N_2 atmosphere. After cooling down followed by washing with DI water various times and drying at 80 °C for 12 h, C-doped CdS@G samples were collected. To examine the thickness of G shell over CdS core and doping of carbon in CdS for photocatalytic H_2 evaluation from water splitting, x mL of GQD (x = 0.05, 0.1, 0.15, 0.2 mL) was added in 300 mg of CdS and 2 mL DI water to obtain the CdS-0.05G, CdS-0.1G, CdS-0.15G, and CdS-0.2G samples, respectively. The content of graphene loading on CdS was measured by coating the 0.05, 0.1, 0.15, 0.2 ml pure GQD on glass slides. After drying the GQD coated glass slides, the amount of graphene was 4.81, 9.70, 14.55 and 19.5 mg.

2.5. Characterization techniques

Powder X-ray diffraction (XRD) was applied to investigate the crystal structure of all the samples using X-ray diffractometer (D8 A25 DaVinci, Bruker) with Cu Kα radiation (λ = 1.54 Å) in 2θ = 10–80° range. The crystallite domain sizes of CdS are calculated applying the Scherrer equation [30] on the (100) diffraction peak. For Ramana analysis, micro-Raman spectrometer (InVia Reflex Spectrometer System, Renishaw) having a laser of 532 nm wavelength was used. The morphological analysis was done using field emission scanning electron microscopy (SEM), (FEI APREO) coupled with an EDX detector (Oxford) and transmission electron microscopy (Jeol JEM 2100 − LaB6) operating at 200 kV. The optical behavior of the as-synthesized photocatalysts was measured by an UV-vis spectrophotometer (NanoDrop UV-vis spectrophotometer, Thermo Fischer) in cuvette arrangement. For absorbance spectra measurements, powder samples were dispersed in ethanol (0.5 mg mL^{-1}). The specific surface area of all samples was measured by a Micromeritics TriStar II 3020 by obtaining the N_2 sorption isotherms at −196 °C. Specific surface area and average pore width of all the samples were estimated by applying the Brunauer–Emmett–Teller (BET) and Barret-Joyner-Halenda (BJH) equations, respectively, on the N_2 adsorption and

desorption isotherms. The surface analysis along with the estimation of valence states of the elements present in the samples was studied using X-ray photoelectron spectroscopy (XPS) (Axis Ultra DLD XP spectrometer, Kratos Analytical) equipped with Al Kα radiation (1486.6 eV). The spectra were recorded using a pass energy of 10 eV. All the data were fitted by CASA XPS software and all peaks were calibrated against the C 1s peak at 284.8 eV.

2.6. Photoelectrochemical measurements

Photoelectrochemical measurements were performed in a standard three-electrode cell using a Princeton Versa STAT potentiostat analyzer (Princeton Applied Research) under illumination with a 150 W Xenon solar simulator (SCIENCETECH SS150) and a SCIENCETECH FRSS air mass (AM) 1.5 global (G) filter. A uniform mixture of as-synthesized photocatalysts was made by sonicating in ethanol (1 mg mL^{-1}) and a uniform layer of properly dispersed catalysts was coated on 1 cm^2 area of fluorine-doped tin oxide (FTO) by the doctor's blade technique. The three-electrode cell is constructed such that the photocatalyst-coated FTO, Pt wire and Ag/AgCl acted as the working electrode, counter electrode and reference electrode, respectively. The electrodes were dipped in 0.1 M Na_2S as electrolyte solution (pH = 13). The chopped photocurrent was measured in dark and light with 20 s interval by without applying any bias. The electrochemical impedance spectroscopy (EIS) is used at 0 V (vs. Ag/AgCl), with AC amplitude of 20 mV in a frequency range of 0.1 mHz–0.2 MHz in dark and light to obtain the Nyquist plots. To locate the valence band potential and carrier density of all the synthesized samples, Mott-Schottky plots were obtained by measuring electrochemical impedance with a frequency of 100–20000 Hz and voltage window of −1.5 to 1 V. The obtained potential (vs. Ag/AgCl) was converted to RHE (NHE, pH = 0) using the Eq. (1) [31] and the carrier density in the semiconductor was calculated by applying Eq. (2) as given below:

$$E_{RHE} = E^{o}_{Ag/AgCl} + 0.059\,pH + E_{Ag/AgCl} \quad (1)$$

$$E^{o}_{Ag/AgCl}(\text{Saturated KCl}) = +0.197\ \text{V at } 20\ ^{\circ}\text{C}$$

$$\frac{1}{C^2} = \frac{2}{\varepsilon\varepsilon_{\circ}A^2eN_D}\left(V - V_{fb} - \frac{K_BT}{e}\right) \quad (2)$$

here A and C is the area and capacitance of the electrode, respectively. ε and ε_o represents the dielectric constant of CdS (8.9), and permittivity of free space, respectively. N_D is the carrier density, e is the electronic charge, T is the absolute temperature, K_B is the Boltzmann's constant, V is the applied bias and V_{fb} represents the flat bandgap of the semiconductor material. The slope of the linear plot of the $1/C^2$ and V gives the N_D, and V_{fb} can be estimated from the intercept on the V axis [32].

2.7. Photocatalytic H_2 generation setup

Tests for photocatalytic H_2 generation from water were carried out in a side irradiated quartz reactor as previously reported [26] and shown in Fig. S1. Typically, 40 mg of photocatalysts were mixed in 600 ml of tap water or deionized water (DI) solution containing 0.125 M Na_2S and 0.175 M Na_2SO_3 which act as sacrificial agents. The photoreactor containing the reactants was sealed, and to remove any dissolved oxygen Ar gas was flown (100 mL min^{-1}) through the reactor for half an hour in the dark. After degassing, the photoreactor was illuminated with simulated solar light from 150 W Xeon solar simulator (SCIENCETECH SS150) at1 sun conditions, with flowing Ar gas. The photogenerated H_2 was estimated from effluent gases of the reactor after every 15 min using an on-line micro-Gas chromatography unit (Agilent Technologies 3000) equipped with Thermal Conductivity Detector (TCD). The average photogenerated H_2 was measured by testing the same sample three times at the same conditions. The apparent quantum efficiency (AQE) was calculated applying Eq. (3) [29], and the detailed calculations steps are shown in the Supplementary data (S1).

$$AQE = \frac{Number\ of\ reacted\ electrons}{Total\ number\ of\ photons\ absorbed} \times 100 \quad (3)$$

The stability of the optimized sample CdS-0.15G was evaluated for photocatalytic H_2 generation for 20 consecutive hours (h) under the identical conditions as reported for regular H_2 generation tests.

3. Results and discussion

3.1. Material synthesis approach

The as-synthesized CdS nanoparticles have a positive surface charge due to the non-stoichiometric Cd and S atomic ratio on the surface of the nanoparticles [33,34]. The surface of graphene quantum dots (GQD) is negatively charged due to the presence of –COOH and C═O groups [35]. During the sonication of CdS nanoparticles and GQD in DI water, the GQD particles are attracted to the surface of CdS particles by electrostatic interaction [35–37]. A continuous layer of graphene (G) is formed around the surface of the CdS nanoparticles to form graphene-wrapped CdS particles (CdS@G) by stacking of GQD utilizing π-π interactions, oxygen-containing groups and dipole–dipole attractions [38,39]. Heat treatment of dried CdS@G samples at 400 °C in N_2 atmosphere causes doping of carbon from the graphene shell to the CdS particles to form C-doped CdS@G nanostructures.

3.2. Morphological analysis

The morphology of pure CdS nanoparticles and optimized C-doped CdS@G sample (CdS-0.15G) was investigated by field emission scanning electron microscopy (FE-SEM) and transmission electron microscopy (TEM) as shown in Fig. 2. Pure CdS particles ~70 nm in size and conical in shape can be

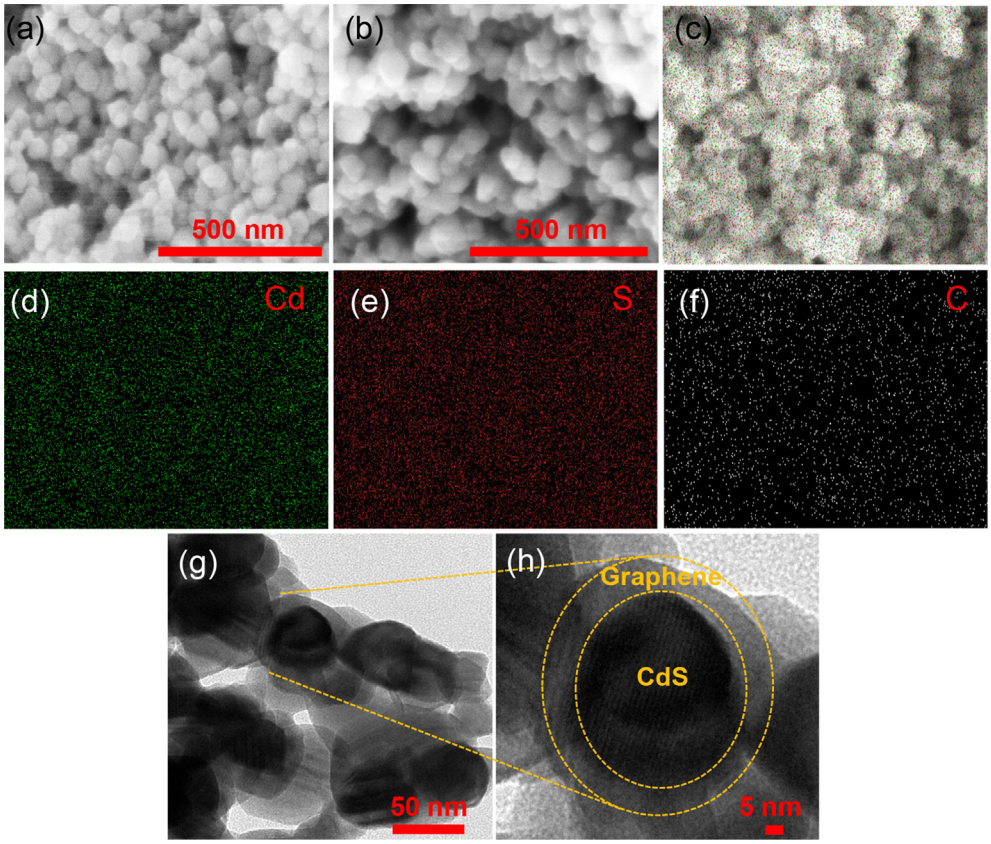

Fig. 2. SEM images of pure CdS nanoparticles (a), CdS-0.15G (b), EDX elemental image of CdS-0.15G (c), Cd (d), S (e), C (f) and TEM images of C-doped CdS@G, i.e., CdS-0.15G sample (g) and enlarged images of (g) showing single particles of C-doped CdS@G (h).

seen in the FE-SEM image Fig. 2a. Fig. 2b shows the SEM image of CdS-0.15G sample having similar morphology as pure CdS nanoparticles. To investigate the presence of carbon content in the CdS-0.15G sample, EDX elemental mapping was performed and shown in Fig. 2c. Fig. 2d,e show the uniform presence of Cd and S in the CdS-0.15G sample and the presence of C on the surface of CdS particles forming the core-shell structure as confirmed by Fig. 2f. Furthermore, a TEM image of CdS-0.15G forming a core-shell structure of C-doped CdS nanoparticles and graphene can be seen in Fig. 2g in which C-doped CdS particles are wrapped with a uniform layer of graphene. Fig. 2h shows an enlarged image of a single particle of C-doped CdS of Fig. 2g which is covered with a graphene layer with a thickness of ~4 nm, confirming the formation of a core-shell structure of C-doped CdS and graphene.

3.3. Crystallite structure

X-ray diffraction (XRD) patterns of pure CdS nanoparticles and various samples of C-doped CdS@G are shown in Fig. 3(a). All samples exhibited sharp and narrow diffraction peaks of pure CdS nanoparticles associated with the wurtzite structure, matching the JCPDS card no. 80-0006 [26,40]. Furthermore, graphene peaks in C-doped CdS@G samples cannot be observed due to the low graphitic content [24]. Fig. 3b shows the extended X-ray diffractograms of pure CdS nanoparticles and the C-doped CdS@G samples. A shift in the (100), (002), (101) peaks toward lower 2θ angles in C-doped CdS@G samples compared to pure CdS was observed, possibly due to lattice expansion caused by the C-doping during heat treatment of the samples during synthesis. As the content of graphene increases by adding 0.05 mL–0.15 mL GQD solution in the C-doped CdS@G samples (CdS-0.05G, CdS-0.1G, and CdS-0.15G), an increase in the 2θ shift towards lower angles is observed. With further increase in the graphene content in CdS-0.2G, the 2θ shift towards lower angles disappeared. The crystallite domain sizes of CdS in all the samples are estimated to be in the range of 35–40 nm (Table S1).

To further investigate the presence of graphene in C-doped CdS@G samples, Raman spectroscopy is used as shown in Fig. 3b,d. Raman analysis of pure CdS nanoparticles shows that the characteristic Raman peaks around 300 cm^{-1} are attributed to the longitudinal optical mode (LO-1) resulting from Cd–S bond vibration from A1 mode and a peak around 600 cm^{-1} exhibits the first overtone of the A1 mode (LO-2) [41]. Raman spectra of C-doped CdS@G samples exhibit the D (1353 cm^{-1}) and G bands (1593 cm^{-1}) not present in pure CdS nanoparticles, which supports the presence of graphene in the C-doped CdS@G samples [42,43]. Fig. 3d shows an enlarged view of Fig. 3c to further investigate the graphene in C-doped CdS@G samples from the intensity of the D band

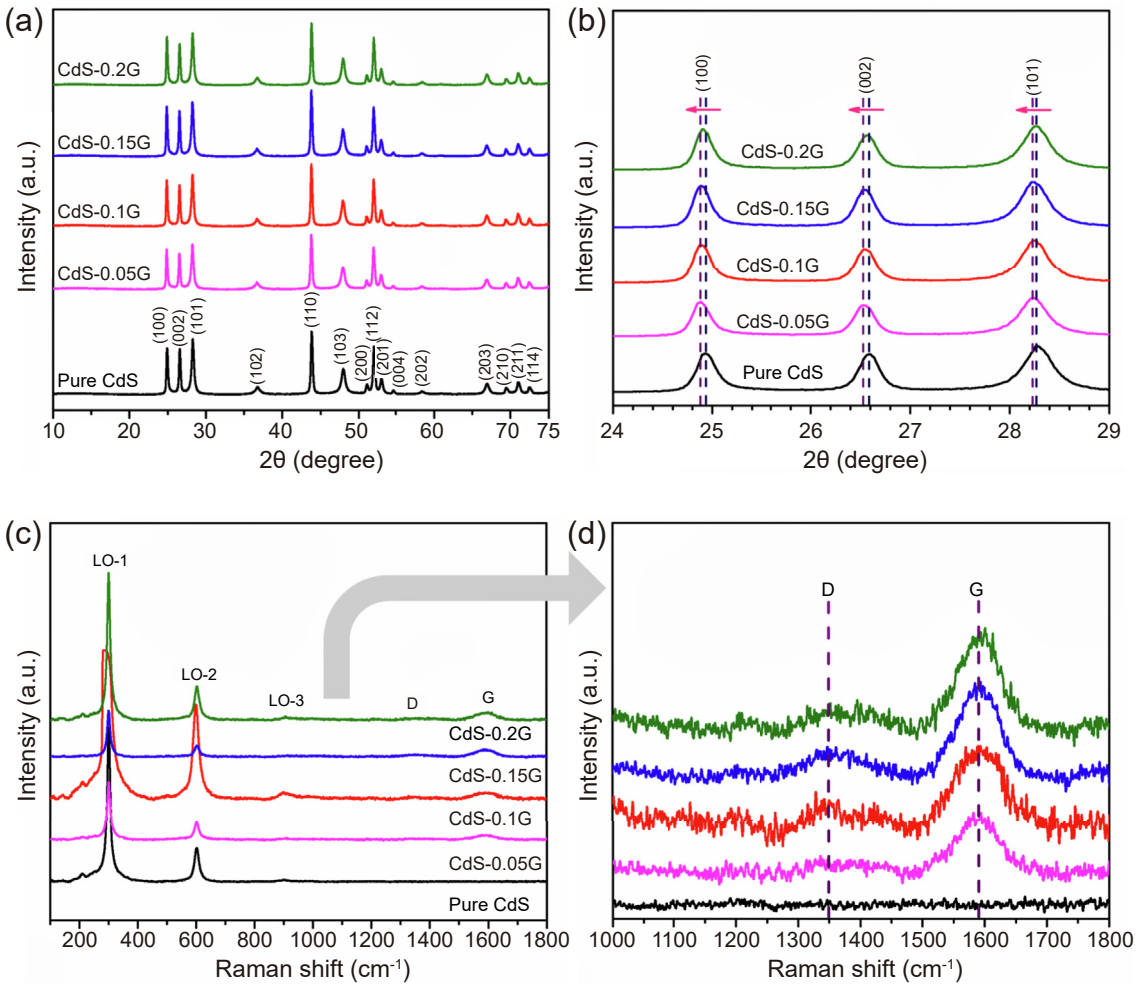

Fig. 3. XRD pattern of pure CdS nanoparticles and C-doped CdS@G samples (a), enlarged view of the XRD pattern (b), Raman spectra of pure CdS nanoparticles and C-doped CdS@G samples (c) and enlarged view of the Raman spectra in the region of the D and G band (d).

(I_D) and G band (I_G). The ratio of I_D to I_G is in the range of 0.32–0.58 (as shown in Table S1) which suggests that there is a large proportion of graphenic carbon (sp^2 carbon network) and defective carbon, confirming the presence of high-quality graphene [44,45] in the C-doped CdS@G samples.

3.4. Textural analysis

Textural properties including specific surface area and pore size distribution of the samples were analyzed by N_2 adsorption–desorption isotherms as shown in Fig. 4a and

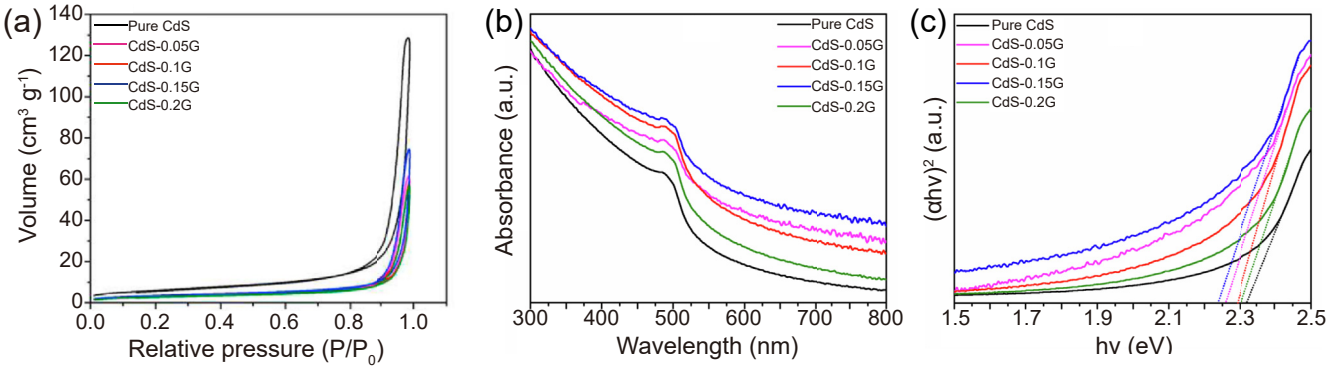

Fig. 4. BET adsorption/desorption isotherms for pure CdS nanoparticles and C-doped CdS@G samples (a), Uv-vis absorption spectra (b) and optical bandgap calculations (c) of pure CdS and C-doped CdS@G samples.

Fig. S2. The shape of all the isotherms is revealing type IV according to the IUPAC classification Fig. 4a [46]. At lower relative pressures, monolayer adsorption is first observed which later continues with the multilayer adsorption shown by a steep rise, followed by capillary condensation taking place in the mesopores of the materials at higher relative pressures [46]. The isotherms show H3 hysteresis loop indicating the presence of slit-like pores [46]. The pure CdS nanoparticles have a surface area of 19 m^2 g^{-1} while all the C-doped CdS@G samples showed slightly lower surface areas, as shown in Table S2. Aggregation of the particles during heat treatments and the slight increase in the particle size by the C-shell on CdS might be the reasons for the decrease in surface area. The BJH pore size distribution of all samples is shown in Fig. S2 and average pore width values are tabulated in Table S2 in which all the samples have pore sizes in the mesoporous range with diameters centered around 40 nm [47].

3.5. Optical properties

To investigate the optical behavior of pure CdS nanoparticles and C-doped CdS@G samples, UV-vis absorption spectra are measured and presented in Fig. 4b. Pure CdS nanoparticles show an absorption onset at *ca.* 500 nm which is due to the intrinsic bandgap transition of electrons from the valence band to the conduction band [48]. The UV-vis absorption spectra of C-doped CdS@G samples exhibited enhanced absorption in the visible and UV regions, and the absorption onset is slightly red-shifted suggesting a decrease in the bandgap compared to pure CdS. This increase in absorption and reduction in bandgap may have a positive effect on the photocatalytic H_2 generation. The bandgap of pure CdS nanoparticles and C-doped CdS@G samples are shown in Fig. 4c which is calculated using the Tauc's relationship obtained by plotting the $(\alpha h\nu)^n$ with respect to the bandgap energy $E_g = h\nu$ (where h is Planck's constant, α is the absorption coefficient, ν is the frequency and $n = 2$ for the direct bandgap nature of CdS) [49,50]. Pure CdS exhibits bandgap energy of 2.32 eV which is close to the reported values of hexagonal CdS. The gradual bandgap narrowing is observed in the C-doped CdS@G samples as the amount of GQD increase in the samples (Table S3), due to the doping of carbon in the CdS matrix, and the interaction of graphene and CdS [51], up to the optimized sample, i.e., CdS-0.15G. With further increase in graphene content in the CdS-0.2G sample, the bandgap narrowing is reduced.

3.6. Surface analysis

The chemical states of the pure CdS and CdS-0.15G samples along with the effect of carbon doping and interaction of graphene with the CdS nanoparticles were further investigated by XPS. For pure CdS, see Fig. 5a, Cd is in the +2 oxidation state with the Cd $3d_{5/2}$ and Cd $3d_{3/2}$ components at 405.1 eV and 411.9 eV, respectively [26,52]. A minor contribution at the high binding energy side of the Cd^{2+} component is attributed to the terminal surface Cd atoms [53]. The corresponding XPS spectra of the S 2p region is shown in Fig. 5b. The S $2p_{3/2}$ and S $2p_{1/2}$ peaks at binding energies 161.5 eV and 162.7 eV, respectively, are consistent with S^{2-} in pure CdS [26,54]. In addition, a minor contribution at higher binding energy is detected, associated with the presence of sulfate groups [55]. For the CdS-0.15 sample, the Cd 3d and S 2p spectra exhibit similar features as pure CdS. However, the peaks are shifted 0.4 eV towards lower binding energies. As the electronegativity of C (2.55) is less than S (2.58), a shift towards lower binding energies is expected compared to pure CdS [56]. Furthermore, the intensities of Cd 3d and S 2p peaks are slightly lower in the CdS-0.15G sample as compared to the spectra of pure CdS, caused by graphene covering the CdS nanoparticles. Fig. 5c shows the raw and deconvoluted XPS spectra of the C 1s region, showing a main component at 284.8 eV, associated with sp^3/sp^2 hybridized carbon (C–C/C═C) present in the graphene. The other three deconvoluted peaks appearing around 286.3 eV, 288.3 eV, and 289.3 eV indicate the presence of hydroxyl, carbonyl, and carboxyl groups on the surface [28].

3.7. Photocatalytic H_2 generation

The photocatalytic activity of all the synthesized samples is investigated for H_2 generation by water splitting under simulated solar light with air mass 1.5 global (AM 1.5G) conditions in the presence of 0.125 M Na_2S and 0.175 M Na_2SO_3 acting as hole scavengers. Fig. 6a shows the rate of H_2 generation from water using pure CdS nanoparticles or C-doped CdS@G samples. During the photocatalytic H_2 generation tests, pure CdS nanoparticles yield 0.67 mmol g^{-1} h^{-1} of hydrogen and the amount of generated H_2 increases with increasing GQD content in C-doped CdS@G samples. Sample CdS-0.15G gives the highest yield of photocatalytic H_2 generation by producing 3.12 mmol g^{-1} h^{-1}, which is ~4.6 times superior to pure CdS nanoparticles. With a further increase in the loading of graphene on CdS nanoparticles, a decrease in the photocatalytic H_2 generation is observed which is due to lower absorption of light by the CdS in the CdS-0.2G sample evident from the UV-vis spectra. Table S2 shows the calculated apparent quantum efficiency (AQE) of all the samples and the most active sample exhibited AQE of 11.7% which is highly promising compared to reported values utilizing similar carbon-based CdS samples (Table S4).

The control tests in the dark of CdS-0.15G samples did not show any photocatalytic hydrogen generation, verifying that the generated H_2 is a result of a photocatalytic reaction. The tap water used in photocatalytic H_2 generation tests may contain impurities possibly affecting the photocatalytic activity. To investigate the role of impurities, present in tap water, control tests with pure CdS nanoparticles in DI water and tap water were performed separately under the same conditions. A similar photocatalytic H_2 generation by using DI water and tap water was obtained as showed in Fig. S3, suggesting that the impurities present in tap water have a negligible effect on the photocatalytic H_2 generation. Thus, the use of tap water for

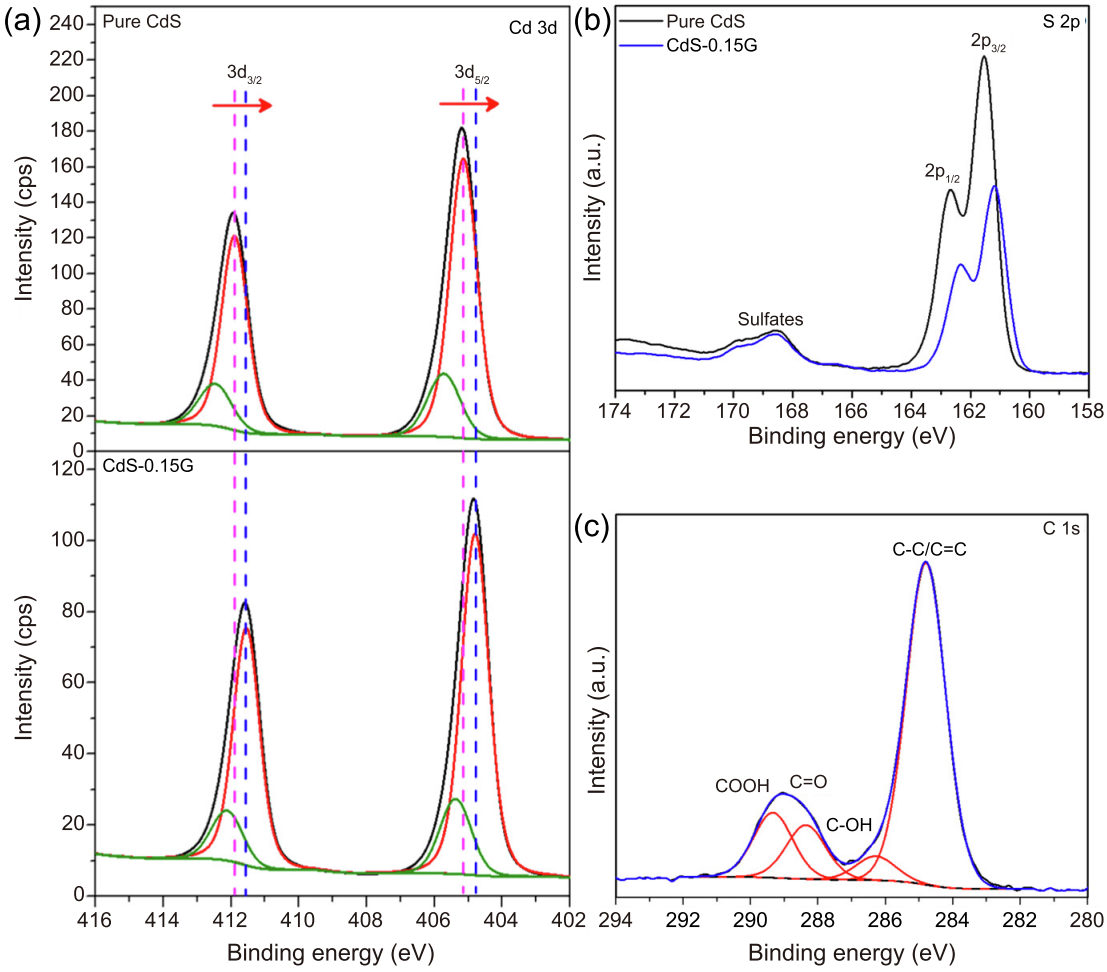

Fig. 5. XPS spectra of Cd 3d of pure CdS and CdS-0.15G samples (a), S 2p (b) of pure CdS and CdS-0.15G samples and C 1s of CdS-0.15G sample (c).

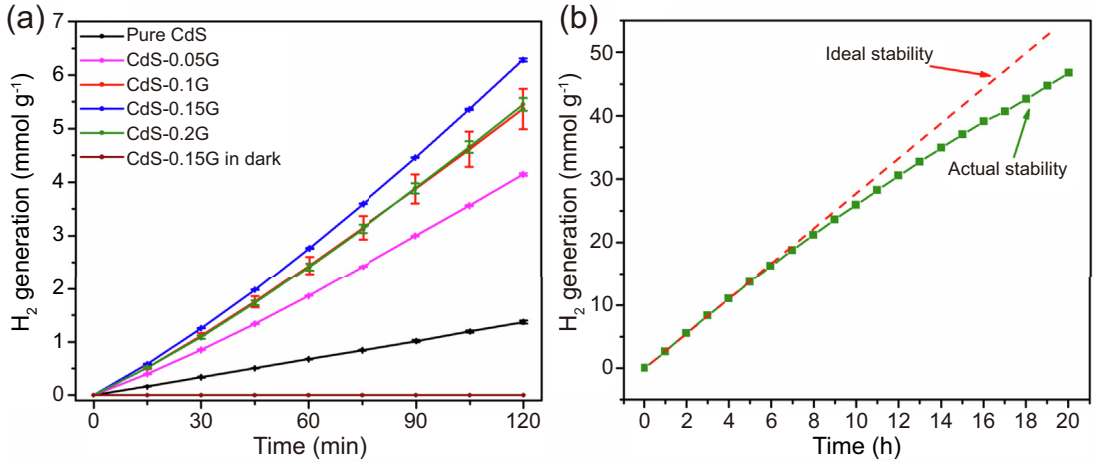

Fig. 6. Rate of H_2 generation from water using pure CdS nanoparticles and C-doped CdS@G samples (a) and stability test employing CdS-0.15G sample (b) using simulated solar illumination with AM 1.5 G conditions.

photocatalytic H_2 generation is more favorable in terms of practical use than DI water. Further control tests were also conducted to confirm that the enhanced photocatalytic H_2 generation by CdS-0.15G is due to the combined effect of the C-doping and the use of graphene as co-catalyst. Fig. S4 shows the amount of photocatalytic H_2 generated

by the CdS-0.15G sample and a CdS-0.15G sample not subjected to heat treatment during the synthesis process. CdS-0.15G (without heat treatment) is without C-doping and this sample generated slightly higher H_2 than pure CdS nanoparticles due to the presence of graphene as co-catalyst, but considerably less than the CdS-0.15G sample. The enhanced photocatalytic H_2 generation obtained from CdS-0.15 is due to a combined effect of C-doping and action of graphene as co-catalyst.

The stability of the most active sample (CdS-0.15G) is tested by performing the photocatalytic H_2 generation continuously for 20 h in the same setup as shown in Fig. 6b. The sample exhibited a relatively stable behavior for photocatalytic hydrogen generation, losing 15% activity after 20 h. The stable behavior of the photocatalysts sample is attributed to the presence of graphene shell over CdS nanoparticles which makes the efficient hole transfer from CdS. These holes are then neutralized by the hole scavenger in the reaction mixture which protects the CdS from photo-corrosion. Furthermore, the graphene shell over CdS protects it from mechanical degradation as well.

3.8. The reaction mechanism for photocatalytic H_2 generation

To investigate the charge transfer mechanism and semiconductor behavior along with the carrier density (N_D), transient photocurrent density and electrochemical impedance were measured. Fig. 7a shows the transient photocurrent density of pure CdS nanoparticles and C-doped CdS@G samples measured in 0.1 M Na_2S solution during on/off illumination. Photocurrent density increases as the graphene layer thickness increase over CdS by increasing the GQDs content up to 4.45 μA cm^{-2} by the CdS-0.15G sample under illumination which indicates that efficient charge transfer occurs from the CdS to the graphene layer leading to higher photocatalytic activity [24]. Further increase in the GQD content results in the formation of a thicker graphene layer which hinders light absorption in CdS. As a result, less generation of electrons (e^-) and holes (h^+) was detected, and hence a decrease in photocurrent density for the CdS-0.2G sample was observed. Fig. 7b shows that the CdS-0.15G sample has the smallest radius of semi-circle in light than the pure CdS nanoparticle and all the

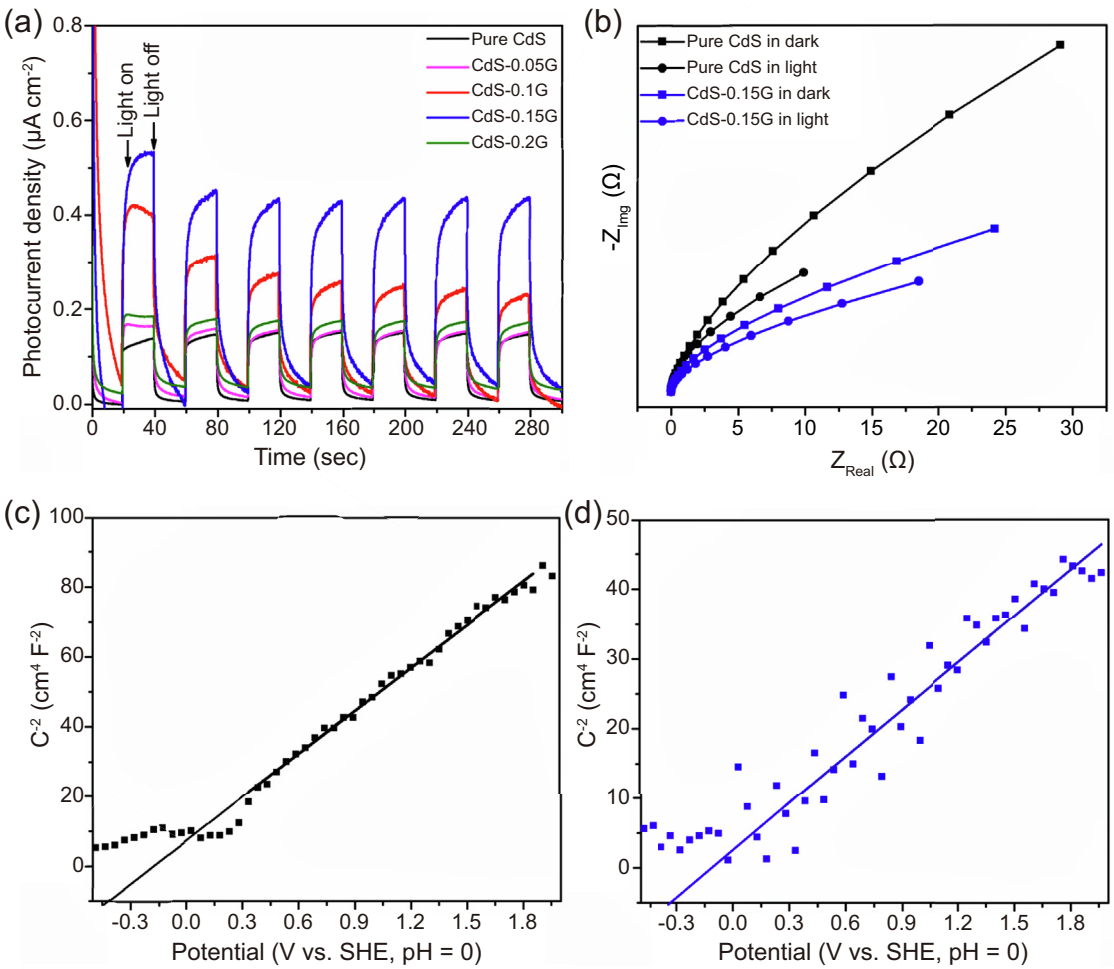

Fig. 7. Chopped photocurrent response of pure CdS and C-doped CdS@G samples (a), Nyquist plots of pure CdS and CdS-0.15G samples in dark and light (b), Mott-Schottky plots of pure CdS nanoparticles (c) and CdS-0.15G (d).

samples in the dark as well (Fig. S5). This indicates that charge carriers experience less overall charge transfer resistance to flow from CdS towards the graphene layer, resulting in improved charge separation efficiency. Fig. 7c,d and Fig. S6 present the Mott-Schottky plots of pure CdS nanoparticles and C-doped CdS@G samples which are used to determine the carrier density (N_D) and flat bandgap of the semiconductors. All the samples exhibited a positive slope of Mott-Schottky plots which shows the n-type behavior of the photocatalysts and in the n-type semiconductors, a flat bandgap potential represents the conduction band potential [31]. The conduction band potential of pure CdS nanoparticles and C-doped CdS@G samples were also estimated by the Mott-Schottky plots as shown in Table S3. Pure CdS exhibited a conduction band potential (E_c) of −0.43 V (vs. RHE) which is close to the reported values for CdS [31]. The doping of carbon and wrapping of the CdS nanoparticles with graphene results in a change in E_c towards less negative values. The most active sample, i.e. CdS-0.15G, shows a conduction band potential around −0.32 V(vs. RHE) and with an increase in the graphene content in CdS the value of the conduction band potential is shifting closer to the redox potential of H^+/H_2. The values of the valence band potential (E_v) of all the samples are calculated by using the bandgap values from UV-vis analysis and E_c values tabulated in Table S3. All the samples have similar valence band potentials which confirm that the doping of carbon in the CdS nanoparticles results in lowering the conduction band potential and therefore narrowing the bandgap. To find the N_D in the samples, the slope of the linear part of the Mott-Schottky plots is estimated as shown in Fig. S7 and Eq. (2) is used. It is observed that with the doping of carbon and wrapping of CdS nanoparticles with graphene, the slope of Mott–Schottky is decreased which increased N_D (Table S3). The increased carrier density is beneficial for efficient charge transfer [57,58] which is one of the reasons for obtaining efficient photocatalytic H_2 generation by the optimized sample (CdS-0.15G). Overall, the enhanced photocatalytic activity of the CdS-0.15G sample is attributed to the enhanced light absorption properties, narrowing of the bandgap, suitable conduction and valence band potential, and relatively larger N_D values compared to the other samples.

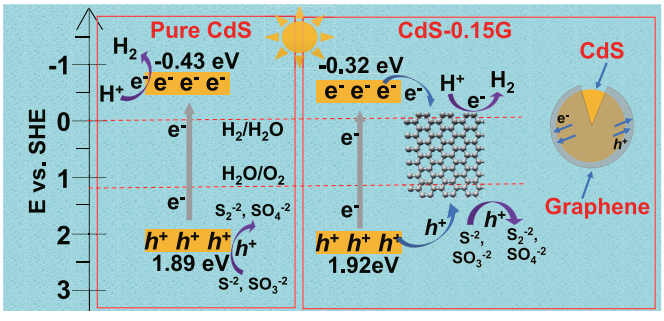

Fig. 8. Proposed illustration of the photocatalytic H_2 generation mechanism from water using pure CdS nanoparticles and the C-doped CdS@G sample.

Based on the experimental findings, we suggest a possible reaction mechanism for photocatalytic H_2 generation as illustrated in Fig. 8. The conduction band potentials of pure CdS and C-doped CdS@G samples are more negative than the work function of graphene quantum dots (ϕ_{GQD}) which lies at −0.08 V vs. RHE [59] while the redox potential for H^+/H_2 has a value of 0 V. In pure CdS nanoparticles, the photocatalytic reaction takes place in the usual manner; under illumination, the e^- and h^+ are generated in the conduction band and valence band. These e^- and h^+ take part in the redox reaction to generate H_2 by reducing the H^+ ions in water, while h^+ is neutralized by the hole scavengers as shown in Fig. 7. In the CdS-0.15G sample, the doped carbon during the synthesis process creates the defect level under the conduction band of CdS which results in narrowing of the bandgap, which in turn increases the solar spectrum absorption. When the reaction mixture is illuminated with the solar simulator, the e^- and h^+ are generated in the conduction band and valence band, respectively. After excitation, the e^- from the conduction band of CdS are transferred to the graphene layer due to the favorable work function of graphene which is acting as the electron extractor. The extracted electrons in the graphene layer then take part in the redox reaction to generate H_2 from water as illustrated in Fig. 7. The h^+ which are generated in the valence band of CdS is also extracted by the graphene layer as the graphene also tends to transport the h^+. These h^+ are neutralized by the hole scavengers in the solution to maintain the charge balance.

3.9. Catalyst deactivation

It is known that CdS can undergo photo-corrosion associated with the holes (h^+) generated in the valence band of CdS during the photochemical reactions, and elemental sulfur is formed in the reaction mixture [3]. To identify possible reasons for the activity loss of CdS-0.15G after the stability test, a range of characterization tools have been applied to analyze the used catalyst (used CdS-0.15G). The TEM image of the used CdS-0.15G sample (Fig. 9a) shows that, after stability tests, the graphene layer is partially removed from the CdS nanoparticles forming a continuous graphite layer and the core-shell structure is destroyed during the photocatalytic H_2 generation tests. The Raman spectrum of the used CdS-0.15G sample (Fig. 9b) shows a similar crystal structure to that of CdS in the fresh CdS-0.15G sample. However, the D band, associated with defects in the graphene, were no longer present in the used CdS-0.15G sample, confirming the formation of graphitic carbon [60]. The XRD analysis of used and fresh CdS-0.15 samples show that the crystalline structure is unaltered. The intensity of the X-ray diffraction peaks of used CdS-0.15G is relatively weak compared to the fresh CdS-0.15G sample indicating that the content of CdS in used CdS-0.15G is reduced due to photo-corrosion of CdS nanoparticles by the photochemical reaction [3]. Based upon post characterization of used CdS-0.15G, we suggest that the deactivation mechanism taking place during the photochemical reaction is a destruction of the core-shell structure of C-

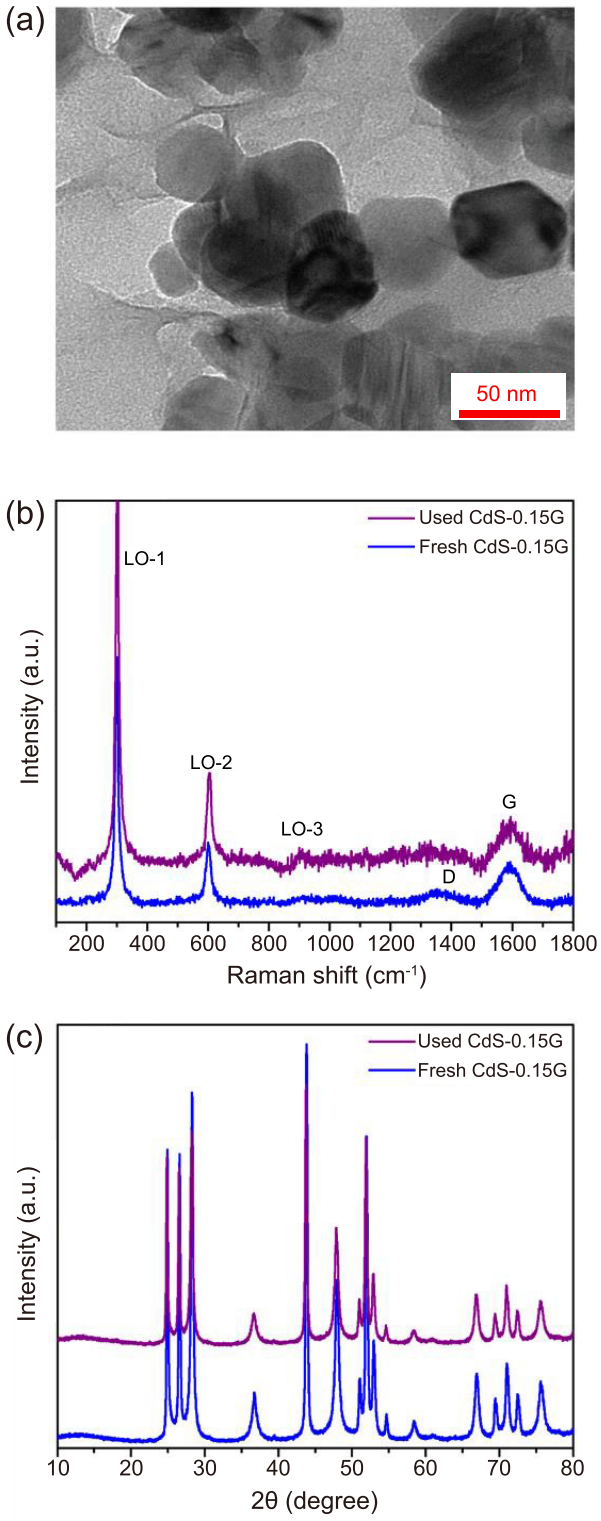

Fig. 9. TEM image (a), Raman analysis (b) and XRD (c) of the used CdS-0.15G sample (after 20 hr stability test).

doped CdS@G. As the graphene layers are removed, the role of graphene as a co-catalysts for CdS nanoparticles vanishes leading to lower photocatalytic activity and stability of CdS nanoparticles [3].

4. Conclusions

We report a facile and unique two-step synthesis method to synthesize C-doped CdS@G samples in which the CdS nanoparticles are wrapped by a thin layer of graphene. The performance of the synthesized C-doped CdS@G samples was investigated towards their ability to generate photocatalytic H_2 from water. The optimized sample CdS-0.15G shows promising H_2 generation under illumination by producing 3.12 mmol g^{-1} h^{-1} H_2, which is ~4.6 times more than pure CdS nanoparticles, giving an AQE of 11.7%. The enhanced and relatively stable performance of the C-doped CdS@G sample is attributed to the broader solar spectrum absorption, narrowing of the CdS bandgap, efficient charge separation by the graphene layer from CdS and sites with enhanced reactivity provided by graphene. Furthermore, the deactivation of the CdS-0.15G sample is investigated after photocatalytic H_2 generation. The decrease in the activity of the sample is attributed to the removal of graphene from the CdS nanoparticles and transition from graphene to graphite and subsequent photodegradation of CdS. The C-doped CdS@G approach seems promising for enhancing the activity of CdS in photocatalytic H_2 generation.

Conflict of interest

The authors declare no conflict of interest.

Acknowledgments

The authors are thankful for the support from the Research Council of Norway provided by the Norwegian Center for Transmission Electron Microscopy, NORTEM (197405/F50) and NTNU NanoLab (grant number 245963) which have provided the characterization tools. The authors also acknowledge the strategic funding support provided by Department of Chemical Engineering, NTNU, Trondheim, Norway.

Appendix A. Supplementary data

Supplementary data to this article can be found online at https://doi.org/10.1016/j.gee.2020.10.017.

References

[1] H. Wang, Z. Jin, X. Hao, Dalton Trans. 48 (2019) 4015–4025.
[2] T. Hisatomi, J. Kubota, K. Domen, Chem. Soc. Rev. 43 (2014) 7520–7535.
[3] V.M. Daskalaki, M. Antoniadou, G. Li Puma, D.I. Kondarides, P. Lianos, Environ. Sci. Technol. 44 (2010) 7200–7205.
[4] Z.R. Tang, B. Han, C. Han, Y.J. Xu, J. Mater. Chem. A 5 (2017) 2387–2410.
[5] Z. Zhang, J. Zhang, N. Chen, L. Qu, Energy Environ. Sci. 5 (2012) 8869–8890.
[6] Q. Li, B. Guo, J. Yu, J. Ran, B. Zhang, H. Yan, J.R. Gong, J. Am. Chem. Soc. 133 (2011) 10878–10884.

[7] W. Han, D. Li, M. Zhang, H. Ximin, X. Duan, S. Liu, S. Wang, J. Hazard Mater. 395 (2020) 122695.
[8] P. Zeng, Q. Zhang, T. Peng, X. Zhang, Phys. Chem. Chem. Phys. 13 (2011) 21496.
[9] C. Zhang, J. Lai, J. Hu, RSC Adv. 5 (2015) 15110–15117.
[10] J. Shi, H. Cui, Z. Liang, X. Lu, Y. Tong, C. Su, H. Liu, Energy Environ. Sci. 4 (2011) 466–470.
[11] H.Y. Chen, S. Maiti, D.H. Son, ACS Nano 6 (2012) 583–591.
[12] J.W. Shi, D. Sun, Y. Zou, D. Ma, C. He, X. Ji, C. Niu, Chem. Eng. J. 364 (2019) 11–19.
[13] R. Shi, H.F. Ye, F. Liang, Z. Wang, K. Li, Y. Weng, Z. Lin, W.F. Fu, C.M. Che, Y. Chen, Adv. Mater. 30 (2018) 1705941.
[14] M. Luo, Y. Liu, J. Hu, H. Liu, J. Li, ACS Appl. Mater. Interfaces 4 (2012) 1813–1821.
[15] P. Wu, J.B. Pan, X.L. Li, X. Hou, J.J. Xu, H.Y. Chen, Chem. A Eur. J. 21 (2015) 5129–5135.
[16] R. Chauhan, A. Kumar, R.P. Chaudhary, Appl. Surf. Sci. 270 (2013) 655–660.
[17] J. Wang, T. Xia, L. Wang, X. Zheng, Z. Qi, C. Gao, J. Zhu, Z. Li, H. Xu, Y. Xiong, Angew. Chem. Int. Ed. 57 (2018) 16447–16451.
[18] D. Yang, S. Xu, Q. Chen, W. Wang, Colloids Surf. A Physicochem. Eng. Asp. 299 (2007) 153–159.
[19] Y. Yang, D. Ni, Y. Yao, Y. Zhong, Y. Ma, J. Yao, RSC Adv. 5 (2015) 93635–93643.
[20] X. Zhang, J. Qin, R. Hao, L. Wang, X. Shen, R. Yu, S. Limpanart, M. Ma, R. Liu, J. Phys. Chem. C 119 (2015) 20544–20554.
[21] G. Poungchan, B. Ksapabutr, M. Panapoy, Mater. Des. 89 (2016) 137–145.
[22] Y. Liu, Y.X. Yu, W.D. Zhang, J. Alloys Compd. 569 (2013) 102–110.
[23] J.C. Orlianges, C. Champeaux, P. Dutheil, A. Catherinot, T.M. Mejean, Thin Solid Films 519 (2011) 7611–7614.
[24] M. Zubair, H. Kim, A. Razzaq, C.A. Grimes, I. S, J. CO_2 Util. 26 (2018) 70–79.
[25] B. He, R. Liu, J. Ren, C. Tang, Y. Zhong, Y. Hu, Langmuir 33 (2017) 6719–6726.
[26] M. Zubair, I.H. Svenum, M. Rønning, J. Yang, Catal. Today 328 (2019) 15–20.
[27] Y. Dong, J. Shao, C. Chen, H. Li, R. Wang, Y. Chi, X. Lin, G. Chen, Carbon 50 (2012) 4738–4743.
[28] S. Wang, Z.G. Chen, I. Cole, Q. Li, Carbon 82 (2015) 304–313.
[29] M. Zubair, I.H. Svenum, M. Rønning, J. Yang, Catalysts 10 (2020) 358.
[30] P. Scherrer, Göttinger Nachrichten Math, Phys 2 (1918) 98–100.
[31] S.J. Hong, S. Lee, J.S. Jang, J.S. Lee, Energy Environ. Sci. 4 (2011) 1781–1787.
[32] K. Gelderman, L. Lee, S.W. Donne, J. Chem. Educ. 84 (2007) 685.
[33] Y.V. Kuznetsova, A.A. Rempel, Inorg. Mater. 51 (2015) 215–219.
[34] S.W. Park, C.P. Huang, J. Colloid Interface Sci. 117 (1987) 431–441.
[35] S. Liu, M.Q. Yang, Y.J. Xu, J. Mater. Chem. A 2 (2014) 430–440.
[36] H. Liu, T. Lv, X. Wu, C. Zhu, Z. Zhu, Appl. Surf. Sci. 305 (2014) 242–246.
[37] L. Kuai, Y. Zhou, W. Tu, P. Li, H. Li, Q. Xu, L. Tang, X. Wang, M. Xiao, Z. Zou, RSC Adv. 5 (2015) 88409–88413.
[38] G. Chen, S. Wu, L. Hui, Y. Zhao, J. Ye, Z. Tan, W. Zeng, Z. Tao, L. Yang, Y. Zhu, Sci. Rep. 6 (2016) 19028.
[39] C. Chen, Q.H. Yang, Y. Yang, W. Lv, Y. Wen, P.X. Hou, M. Wang, H.M. Cheng, Adv. Mater. 21 (2009) 3007–3011.
[40] S.E. Haque, B. Ramdas, A. Sheela, N. Padmavathy, Micro Nano Lett. 9 (2014) 731–735.
[41] Y. Liang, L. Zhai, X. Zhao, D. Xu, J. Phys. Chem. B 109 (2005) 7120–7123.
[42] M.E. Khan, M.M. Khan, M.H. Cho, J. Colloid Interface Sci. 482 (2016) 221–232.
[43] M.E. Khan, M.M. Khan, M.H. Cho, RSC Adv. 5 (2015) 26897–26904.
[44] A. Pulido, P. Concepción, M. Boronat, C. Botas, P. Alvarez, R. Menendez, A. Corma, J. Mater. Chem. 22 (2012) 51–56.
[45] A.A. Dubale, W.N. Su, A.G. Tamirat, C.J. Pan, B.A. Aragaw, H.M. Chen, C.H. Chen, B.J. Hwang, J. Mater. Chem. A 2 (2014) 18383–18397.
[46] M. Kruk, M. Jaroniec, Chem. Mater. 13 (2001) 3169–3183.
[47] K.S.W. Sing, D.H. Everett, R.A.W. Haul, L. Moscou, R.A. Pierotti, J. Rouquerol, T. Siemieniewska, Pure Appl. Chem. 57 (1985) 603–619.
[48] Y. Wang, Y. Wang, R. Xu, J. Phys. Chem. C 117 (2013) 783–790.
[49] J. Tauc, R. Grigorovici, A. Vancu, Phys. Status Solidi 15 (1966) 627–637.
[50] L. Zhang, X. Fu, S. Meng, X. Jiang, J. Wang, S. Chen, J. Mater. Chem. A 3 (2015) 23732–23742.
[51] S. Liu, Z. Chen, N. Zhang, Z.R. Tang, Y.J. Xu, J. Phys. Chem. C 117 (2013) 8251–8261.
[52] L. Wu, J.C. Yu, X. Fu, J. Mol. Catal. A Chem. 244 (2006) 25–32.
[53] H.H.Y. Wei, C.M. Evans, B.D. Swartz, A.J. Neukirch, J. Young, O.V. Prezhdo, T.D. Krauss, Nano Lett. 12 (2012) 4465–4471.
[54] N. Zhang, S. Liu, X. Fu, Y.J. Xu, J. Mater. Chem. 22 (2012) 5042.
[55] M. Fantauzzi, B. Elsener, D. Atzei, A. Rigoldi, A. Rossi, RSC Adv. 5 (2015) 75953–75963.
[56] J.Y. Kim, Y.J. Jang, J. Park, J. Kim, J.S. Kang, D.Y. Chung, Y.E. Sung, C. Lee, J.S. Lee, M.J. Ko, Appl. Catal. B Environ. 227 (2018) 409–417.
[57] S.A. Bakar, C. Ribeiro, RSC Adv. 6 (2016) 36516–36527.
[58] Y. Zhou, G. Chen, Y. Yu, L. Zhao, Q. Yu, Q. He, Catal. Sci. Technol. 6 (2016) 1033–1041.
[59] Q. Xiang, J. Yu, M. Jaroniec, J. Am. Chem. Soc. 134 (2012) 6575–6578.
[60] Y. Zheng, A. Wang, Z. Wang, L. Fu, F. Peng, Mater. Res. 20 (2016) 15–20.